

1 **The 2020 M_w 6.8 Elazığ (Turkey) earthquake reveals**
2 **rupture behavior of the East Anatolian Fault**

3 **Léa Pousse-Beltran¹, Edwin Nissen¹, Eric A. Bergman², Musavver Didem**
4 **Cambaz³, Élyse Gaudreau¹, Ezgi Karasözen⁴, and Fengzhou Tan¹**

5 ¹School of Earth and Ocean Sciences, University of Victoria, Victoria BC, Canada

6 ²Global Seismological Services, Golden CO, USA

7 ³Kandilli Observatory and Earthquake Research Institute, Boğaziçi University, İstanbul, Turkey

8 ⁴Alaska Earthquake Center, University of Alaska Fairbanks, Fairbanks AK, USA

9 **Key Points:**

- 10 • The mainshock propagated mostly westwards from a nucleation point on an abrupt
11 ~10° fault bend
- 12 • Only one rupture termination corresponds to an established EAF segment bound-
13 ary, and the rupture may partially overlap with an 1874 earthquake
- 14 • The mainshock exhibits a pronounced shallow slip deficit, that is not fully recov-
15 ered through early shallow afterslip

16 Keywords : earthquake, Turkey, geodesy, seismology

Corresponding author: Léa Pousse-Beltran, leapousse@uvic.ca

Abstract

The 2020 M_w 6.8 Elazığ earthquake was the largest along the Eastern Anatolian Fault (EAF) in over a century, providing valuable insights into its rupture behavior. We use satellite geodesy and seismology to detail the mainshock rupture, postseismic deformation and aftershocks. The mainshock propagated mostly westwards at ~ 2 km/s from a nucleation point on an abrupt $\sim 10^\circ$ fault bend. Only one end of the rupture corresponds to an established EAF segment boundary, and the earthquake may have propagated into the slip zone of the 1874 $M \sim 7.1$ Gölcük Gölü earthquake. It exhibits a pronounced ($\sim 80\%$) shallow slip deficit, only a small proportion of which is recovered by early aseismic afterslip. The slow rupture velocity, shallow slip deficit and low afterslip are characteristic of earthquakes hosted by faults of low-to-intermediate structural maturity, indicating that faults continue to evolve in important ways even as they accrue cumulative offsets of tens of kilometers.

Plain Language Summary

We investigate the 2020 M_w 6.8 Elazığ (Turkey) earthquake, the largest along the Eastern Anatolian Fault in over a century. Anatolian faults are emblematic within the earthquake science community, but most attention has focused on the North Anatolian fault which ruptured repeatedly during the 20th Century, and relatively little is known about the East Anatolian Fault. We use satellite geodesy and seismology to map fault motions during the earthquake, after the earthquake, and in its aftershock sequence. Documenting relations between this earthquake, previous earthquakes, and early postseismic deformation is pivotal to gain a better understanding in what drives rupture behavior. Our results show that previous structural models of the EAF were only partially successful in predicting the end points of the 2020 rupture, and that many aspects of this earthquake are characteristic of structurally immature faults. These results are important for seismic hazard assessment in this region.

1 Introduction

The ~ 500 km-long, left-lateral East Anatolian Fault (EAF) in southeastern Turkey forms the active plate boundary between Arabia and Anatolia (Figure 1a, b). The \sim WSW-trending EAF encompasses several releasing and restraining bends and stepovers (Arpat & Şaroğlu, 1972; Bozkurt, 2001), segmentation that may be influenced by its obliquity

48 to E–W structures of the SE Anatolia Thrust Zone, part of the Bitlis-Zagros suture (Şengör
49 & Yilmaz, 1981; Yilmaz, 1993). Together with the conjugate, right-lateral North Ana-
50 tolian Fault (NAF), the EAF accommodates westward extrusion of Anatolia from the
51 Arabia-Eurasia collision zone at a slip-rate of ~ 11 mm/yr (Cetin et al., 2003; Walters
52 et al., 2014; Aktug et al., 2016). Both faults are associated with numerous destructive
53 historical earthquakes (Ambraseys & Jackson, 1998), but whereas the NAF hosted twelve
54 $M_w \geq 6.7$ ruptures during the past century (e.g., A. Barka, 1996; Tibi et al., 2001), the
55 EAF has a notable scarcity of large instrumental events. This hampers our understand-
56 ing of its kinematics, structural characteristics and rupture behavior.

57 The January 24 2020 M_w 6.8 Elazığ earthquake struck at 17:55 UTC (20:55 local
58 time), causing damage across the southern Elazığ and Malatya provinces, killing ~ 41 peo-
59 ple and injuring $\sim 1,600$ others (Çetin et al., 2020). It was the largest EAF earthquake
60 in more than a century, motivating a detailed examination of its rupture characteristics.
61 Nucleating close to Lake Hazar — a contested EAF segment boundary (Figure 1c) —
62 it could help resolve uncertainties in local fault structure and its controls on rupture prop-
63 agation (A. A. Barka & Kadinsky-Cade, 1988; Aksoy et al., 2007; Garcia Moreno et al.,
64 2011; Duman & Emre, 2013). Furthermore, its relations to large historical ruptures in
65 1874 and 1875 (to the NE) and 1893 and 1905 (to the SW) (Ambraseys (1989); Figure 1c)
66 could provide an informative test of the characteristic earthquake and seismic gap mod-
67 els (McCann et al., 1979; Schwartz & Coppersmith, 1984; Kagan et al., 2012). Document-
68 ing the surface expression of the Elazığ earthquake also provides important context to
69 paleoseismic studies of the EAF (Cetin et al., 2003; Garcia Moreno et al., 2011; Hubert-
70 Ferrari et al., 2020).

71 The Elazığ earthquake is potentially of even broader significance. In recent years,
72 a number of studies have linked various earthquake rupture properties to the structural
73 maturity of the host faults, defined here as the degree of advancement in the evolution
74 of its structural properties at kilometeric length scales (Wesnousky, 1988; Manighetti et
75 al., 2007; Dolan & Haravitch, 2014; Perrin et al., 2016). (We acknowledge that struc-
76 tural maturity is often conceptualized at smaller spatial scales and that a range of other
77 definitions exist, e.g. Shelef and Oskin (2010); Brodsky et al. (2011); H. M. Savage and
78 Brodsky (2011)). The central EAF has cumulative geomorphological or geological off-
79 sets of ~ 9 – 26 km, making it of low-to-intermediate structural maturity according to the
80 criteria of both Manighetti et al. (2007) and Dolan and Haravitch (2014). The Elazığ

81 earthquake could therefore help refine relations between fault structural maturity and
82 characteristics such as rupture velocity, off-fault deformation, shallow slip deficits, and
83 afterslip (e.g., Dolan & Haravitch, 2014; Socquet et al., 2019; Li et al., 2020).

84 The main goal of this paper is to characterize the Elazığ mainshock faulting, its
85 early aftershock activity and postseismic deformation. We use Interferometric Synthetic
86 Aperture Radar (InSAR) and optical satellite imagery, teleseismic back-projections, re-
87 gional moment tensors and calibrated hypocentral relocations. We go on to discuss re-
88 lations between the 2020 earthquake and proposed EAF segment boundaries, historical
89 ruptures, and background seismicity. Finally, we assess our results in the context of emerg-
90 ing conceptual models for fault rupture behaviour and consider implications for future
91 earthquake potential along the EAF.

92 **2 Methods**

93 **2.1 Satellite geodesy**

94 We investigated coseismic deformation using European Space Agency (ESA) Sentinel-
95 1 interferograms collected on January 21–22 and 27–28 2020 on ascending tracks 43A
96 and 116A and descending tracks 21D and 123D (Supplementary Table S1). Interfero-
97 grams were processed in GAMMA and unwrapped using the branch-cut algorithm; un-
98 wrapping errors were then manually fixed. We estimated the mainshock fault geometry
99 and slip distribution using a well-established elastic dislocation modeling approach (e.g.,
100 Wright et al., 1999; Elliott et al., 2012) based upon Okada’s (1985) formulae. The un-
101 wrapped interferograms were first downsampled using a Quadtree algorithm (Jónsson
102 et al., 2002). We then used Powell’s minimization algorithm (Press et al., 1992) to solve
103 for the minimum misfit strike, dip, rake, slip, latitude, longitude, length and top and bot-
104 tom depths of a rectangular fault plane embedded within an elastic half-space (Supple-
105 mentary Text S1), as well as E–W and N–S orbital ramps and the zero displacement level.
106 Local minima are avoided by repeating the inversion hundreds of times with randomly-
107 sampled starting parameters and retaining only the lowest residual solution (Clarke et
108 al., 1997; Wright et al., 1999). Ascending and descending data were weighted equally in
109 the inversion, but track 21D was weighted one third relative to 123D since it only spans
110 that fraction of the rupture. We found that two model faults were needed to match the
111 observed displacements well, but that fixing these faults to the observed EAF surface

112 trace produced worse misfits than free location solutions (Supplementary Text S1, Fig-
113 ures S1–S4, and Table S2). We then extended and subdivided these model fault planes
114 into 3×3 km subfaults and solved for the slip distribution. We applied a Laplacian smooth-
115 ing operator and assessed misfits using the L-curve criterion in order to determine the
116 appropriate degree of smoothing (Wright et al., 2003).

117 To investigate early postseismic deformation, we processed four consecutive, 6 day
118 interferograms on each of the four available tracks, starting with the earliest postseis-
119 mic scenes on January 27–28 2020 (Figure S5). These revealed afterslip localized along
120 the fault trace, but the relatively low signal-to-noise ratio precluded us applying the same
121 inversion procedure as for coseismic slip. To quantify afterslip, we first estimated east
122 and vertical displacement components from tracks 43A and 123D, InSAR being largely
123 insensitive to north–south motion (Wright et al., 2004). Observing no clear vertical dis-
124 placement gradient localized along the fault (Figure S6a), we assume that the east com-
125 ponent reflects fault-parallel, not fault-normal, displacement. We projected the east com-
126 ponent onto the 244° -oriented fault and then constructed ~ 8 km-long fault-perpendicular
127 profiles at intervals along strike. On each profile, we modelled displacement (y) at per-
128 pendicular distance (x) with an arctan function to solve for uniform slip U and locking
129 depth D (J. C. Savage & Burford, 1973). Adding a linear term ($R \times x$) to account for
130 residual orbital ramps, we obtained a function model $y = \frac{U}{\pi} \times \arctan(\frac{x}{D}) + Rx$, that
131 we fitted using the least squares Levenberg-Marquardt algorithm (Moré, 1978).

132 We also investigated horizontal surface deformation using an optical image corre-
133 lation (OIC) of pre- and post-earthquake 10 m-resolution ESA Sentinel-2 images and the
134 Cosi-CORR software (Leprince et al., 2007). OIC can detect near-fault surface defor-
135 mation caused by shallow slip in regions where radar interferograms often decorrelate,
136 and can thus help refine InSAR slip models (Xu et al., 2016). Unfortunately, the epicen-
137 tral region was obscured by dense cloud cover after the earthquake with the earliest us-
138 able post-seismic image collected on February 27 2020; our results therefore capture both
139 coseismic and five weeks of postseismic deformation. The pre-event image was acquired
140 on November 9 2019. Processing details are provided in Supplementary Text S2.

141 2.2 Seismology

142 We imaged the mainshock rupture propagation using a phase-weighted relative back
143 projection of high-frequency P waves recorded across a teleseismic station array (Ishii
144 et al., 2005; F. Tan et al., 2019). After trials with data from a number of regions, we chose
145 an Alaskan array of 119 stations at distances of 69–86° and with high cross-correlation
146 coefficients for the first few seconds of the P wave. Theoretical travel times were calcu-
147 lated from a grid of nodes across the source region to each station (Supplementary Text S3)
148 and waveforms were cleaned with a 0.3–2 Hz band-pass filter. Assuming a source depth
149 of 6 km — consistent with our InSAR modeling results — we mapped relative energy
150 at 1 s intervals and a 10 s sliding window for the duration of the rupture.

151 We estimated source mechanisms of early aftershocks (up to February 17 2020) by
152 modeling regional waveforms recorded at distances of 50–380 km by stations of the Kandilli
153 Observatory and Earthquake Research Institute (KOERI; Boğaziçi University Kandilli
154 Observatory and Earthquake Research Institute (2001)) and Disaster and Emergency
155 Management Authority of Turkey (AFAD) seismic networks (Figure 1b). Thirty events
156 were studied, of which half yielded robust, stable solutions. Between 6 and 20 stations
157 were used for each event, yielding azimuthal gaps of at most 140°. Seismograms were
158 filtered between 0.02–0.09 Hz, with the exact frequency band for each event selected af-
159 ter analyzing signal-to-noise ratios and station epicentral distances. Green’s functions
160 were estimated for the local velocity model (Supplementary Text S3) using the discrete
161 wavenumber method (Bouchon, 1981). We solved for the best point source moment ten-
162 sor by minimizing misfits between observed and synthetic waveforms using an iterative
163 deconvolution inversion (Kikuchi & Kanamori, 1991) implemented in the ISOLA soft-
164 ware package (E. N. Sokos & Zahradník, 2008). The fifteen robust solutions (listed in
165 Supplementary Table S3) each meet the variance reduction and other quality criteria de-
166 fined by Zahradník and Sokos (2018); one is shown as an example in Supplementary Fig-
167 ure S8.

168 Finally, we used local, regional and teleseismic phase arrivals to relocate hypocen-
169 ters of the mainshock, 30 early aftershocks (up to February 20 2020), and ~300 well-recorded
170 background events starting in 1971. Data were gathered from regional networks oper-
171 ated by KOERI, AFAD, and the European-Mediterranean Seismological Centre (EMSC),
172 and from the International Seismological Centre (ISC) bulletin. Target earthquakes were

173 separated into five clusters: the first focused on the 2020 sequence and nearby seismic-
 174 ity in 2019; a second targeted earlier events along the Pürtürge EAF segment; and a third,
 175 fourth and fifth covered segments to the ENE and WSW (Supplementary Figure S9a).
 176 Each cluster was relocated using the *mloc* program (Bergman & Solomon, 1990; Walker
 177 et al., 2011), which separates the relocation into two distinct inverse problems reliant on
 178 customized phase arrival time data (Jordan & Sverdrup, 1981). Firstly, arrival times of
 179 all phases at all distances were used to determine cluster vectors that relate individual
 180 locations and origin times to the hypocentroid (the geometrical mean for all events), with
 181 90% confidence usually in the range ~ 1 – 2 km. Secondly, direct *Pg* and *Sg* phases at epi-
 182 central distances of $< 1^\circ$ (Figure 1b) were used to establish the absolute location and ori-
 183 gin time of the hypocentroid, with uncertainties of < 1 km. Combining these steps yields
 184 ‘calibrated’ hypocenters and uncertainties, listed in Table S4. Bespoke crustal velocity
 185 models were determined for each cluster by analyzing fits to *Pg* and *Pn* at the closest
 186 stations and *Pn* and *Sn* at regional distances (Supplementary Text S3 and Figure S9b).

187 **3 Results**

188 **3.1 Background seismicity and foreshock activity**

189 Of the background events relocated to the Pürtürge segment of the EAF, eight are
 190 sufficiently large (M_w 4.9–5.7) as to be ascribed teleseismic focal mechanisms (Figures 1b–
 191 c, Figure 2a). Four of these have predominantly strike-slip mechanisms and form a lin-
 192 ear trend ~ 5 km north of the main fault surface trace. Since this distance exceeds re-
 193 location uncertainties, we suggest either that the Pürtürge segment dips northwards, with
 194 these events nucleating near the base of the fault, or that a previously-unrecognized north-
 195 ern EAF strand crosses this area. We also observe one moderate and several smaller earth-
 196 quakes south of the town of Sivrice, consistent with a minor, southern splay fault observed
 197 by Bulut et al. (2012). The largest of these has a normal faulting mechanism, perhaps
 198 related to development of Lake Hazar basin (Aksoy et al., 2007; Garcia Moreno et al.,
 199 2011; Duman & Emre, 2013).

200 The most recent of the focal mechanism events — on April 4 2019 (M_w 5.3) and
 201 December 27 2019 (M_w 4.9) — are each located within ~ 5 km of the 2020 Elazığ main-
 202 shock epicenter, and so we classify them as foreshocks (Figure 2a,c). Calibrated focal depths
 203 along the Pürtürge segment range from 4–18 km with a peak at 10–13 km (inset to Fig-

204 ure 2c), in close agreement with previous regional studies (O. Tan et al., 2011; Bulut et
 205 al., 2012) and consistent with a central EAF locking depth of ~ 15 km inferred from satel-
 206 lite geodesy (Walters et al., 2014; Aktug et al., 2016).

207 **3.2 Mainshock coseismic faulting**

208 Coseismic interferograms exhibit larger northern and smaller southern fringe lobes
 209 that close near Sivrice in the ENE and near Pürtürge in the WSW (Figure 3a). Invert-
 210 ing the unwrapped interferograms, we obtained two co-linear model faults with strike
 211 244° (Figure 2b, c). The ~ 36 km-long eastern model fault dips 80° N and is left-lateral
 212 (rake 3°), while the ~ 15 km-long western fault dips 64° N and has a small normal com-
 213 ponent (rake -18°). These northward dips are required to match the distinct asymme-
 214 try to the fringe pattern and are consistent with the range of published seismological mech-
 215 anisms (Table 1).

216 At the surface, our model faulting resembles the mapped trace of the EAF (Duman
 217 & Emre, 2013), except that the observed $\sim 10^\circ$ fault bend is manifest in our model as
 218 a small left stepover. Attempts at fixing the model fault surface projection to the ob-
 219 served, kinked surface trace resulted in worse misfits, and so we consider our geometry
 220 to be the best approximation of fault structure at the scale of the seismogenic zone. Nev-
 221 ertheless, the model fault geometry in the region of intersection may reflect limitations
 222 to the modeling approach as opposed to a real segment boundary; instead, the faulting
 223 may ‘twist’ gradually from steeper dips in the east to gentler ones in the west. Maximum
 224 slip of 2.4 m occurs close to the model fault intersection at 6–9 km depth and only < 0.5 m
 225 slip reaches the shallowest patches (Figure 3c). Though the resolution of the shallow-
 226 est slip is limited by InSAR decorrelation along the surface trace, these results are con-
 227 sistent with the absence of primary surface rupturing observed in preliminary field in-
 228 vestigations (Çetin et al., 2020) and suggest a pronounced shallow slip deficit.

229 The InSAR model moment of 1.79×10^{19} Nm (M_w 6.8) closely matches the Global
 230 Centroid Moment Tensor (GCMT) seismic moment of 1.77×10^{19} Nm, implying that
 231 most the slip inferred from InSAR occurred coseismically. Our relocated hypocenter lies
 232 midway along the eastern model fault segment at a depth of ~ 8 km (Figure 2c). $\sim 80\%$
 233 of the InSAR model moment occurs WSW of the epicenter, and only $\sim 20\%$ ENE of it.
 234 Back projection results show that high frequency energy is also released almost exclu-

235 sively WSW of the epicenter, consistent with a rupture velocity in that direction of ~ 2 km/s
236 and a rupture duration of ~ 20 s (Figure 2b). Using high-rate Global Navigation Satel-
237 lite System (GNSS) recordings, Melgar et al. (2020) found similar results (a rupture ve-
238 locity of 2.2 km/s and duration of 20 s). A single peak in back-projected energy a few
239 kilometers ENE of the epicenter matches a local peak in InSAR model slip and confirms
240 that the rupture is not entirely unilateral. However, the smaller (< 0.5 m) coseismic slip
241 resolved by InSAR at the far ENE end of the rupture is below the resolution of the back
242 projection method (F. Tan et al., 2019).

243 **3.3 Postseismic displacements**

244 We observe a sharp phase jump localized on the EAF in the earliest postseismic
245 6 day interferogram (January 27/28 to February 2/3). Although later interferograms suf-
246 fer from decorrelation, this phase jump seems to have disappeared by the time of the last
247 pair processed (February 14/15 to 20/21). We used the cumulative 24 day interferograms
248 (January 28–February 21) to estimate early postseismic afterslip, focusing WSW of the
249 mainshock epicenter where coseismic slip was greatest and where InSAR near-field dis-
250 placements are most coherent (Figure 4a). Fitting fault-perpendicular profiles with the
251 arctan model, we estimate maximum afterslip of ~ 15 cm, less than 7% of the peak co-
252 seismic slip (Figure 4b). The greatest afterslip occurs close to the mainshock epicenter
253 and appears to be buried, with minimum misfit locking depths of ~ 1 km. WSW of the
254 epicenter, afterslip decreases rapidly to ~ 2 –3 cm and the locking depth diminishes to near
255 zero, indicating postseismic surface rupturing.

256 Horizontal coseismic and postseismic displacements mapped with OIC are dom-
257 inated by topographic artefacts without a clear coseismic signal, although a long-wavelength
258 signal near the fault in the E-W displacement field may reflect left-lateral slip (Figure
259 4c). Displacement measurement uncertainties are ~ 0.75 m in the East-West component
260 and ~ 1.0 m in the North-South component (Supplementary Text S2). The lack of a dis-
261 tinct coseismic signal at this resolution is consistent with the pronounced shallow slip
262 deficit inferred from our coseismic and postseismic InSAR models.

3.4 Aftershock seismicity

Most aftershocks exhibit left-lateral mechanisms along or parallel to the EAF (Figure 2c). We observe notable clusters close to the mainshock hypocenter and at either end of the coseismic faulting (near Lake Hazar and Pürtürge). In contrast, very few aftershocks are associated with peak coseismic slip near the InSAR model fault intersection (Figures 2c and 3b). Many of the aftershocks — particularly within the concentrations at either end of the mainshock rupture — lie up to ~ 10 km off the main trace of the EAF, suggesting activation of secondary faults within a damage zone (Liu et al., 2003). Almost all lie north of the EAF surface trace, consistent with the aftershock distribution obtained by Melgar et al. (2020) and with the inferred northward fault dip. The easternmost aftershock studied here has a distinctive normal component, consistent with interpretations of the Lake Hazar basin as a releasing bend or pull-apart (Aksoy et al., 2007; Garcia Moreno et al., 2011; Duman & Emre, 2013).

Aftershock relocated focal depths range from 7–17 km whereas centroid depths from waveform modeling are 2–13 km (inset to Figure 2c). Use of an alternative velocity model (Acarel et al., 2019) increased waveform model centroid depths by on average ~ 2 km, reducing but not eliminating this discrepancy. These results mimic relations observed in comparably-instrumented regions elsewhere (Karasözen et al., 2016, 2018; Gaudreau et al., 2019) and likely reflect the depth resolution limitations of both methods, together with the propensity for earthquakes to nucleate deeper within the seismogenic zone and rupture upwards.

4 Discussion

4.1 Relations with previous seismicity and with structural segmentation of the EAF

The Elazığ mainshock nucleated in a zone of apparent structural complexity between the villages of Uslu and Doğanyol, where Duman and Emre (2013) mapped a pair of small (< 500 m) right steps and an abrupt bend in the EAF surface trace (Figure 2c). The eastern right step (at Uslu) is manifest as a ~ 1 km fault gap and the western right step (north of the Karakaya reservoir) as a ~ 4 km stretch of parallel, overlapping fault strands. Just west of these parallel strands, the EAF abruptly changes strike by $\sim 10^\circ$. The April 4 and December 27 2019 foreshocks provide further evidence of structural com-

294 plexity in this area (Figure 2a). The April 4 M_w 5.3 foreshock likely ruptured the EAF
295 close to the eastern fault step at Uslu. The December 27 M_w 4.9 foreshock was located
296 at the fault bend north of Doğanyol; both its nodal planes are at high angles to the EAF,
297 suggesting rupture of a subsidiary structure or splay.

298 The 2020 mainshock nucleated within this zone of complexity, between the two fore-
299 shocks (Figure 2b, c). Towards the ENE, the mainshock terminated at Lake Hazar, in-
300 terpreted by Cetin et al. (2003) and Duman and Emre (2013) as a left-stepping releas-
301 ing bend, by Aksoy et al. (2007) as a horst structure, and by Garcia Moreno et al. (2011)
302 as a continuous, unsegmented fault section. Towards the WNW, it propagated past the
303 $\sim 10^\circ$ fault bend — manifest in our simplified slip model as a releasing step — to ter-
304 minate on a relatively straight section of the fault west of Pürtürge. Here, our model fault
305 geometry is slightly oblique to the mapped surface trace, hinting that at the scale of the
306 seismogenic zone the fault has a somewhat skewed, non-planar geometry (Diederichs et
307 al., 2019).

308 Large historical earthquakes in 1874, 1875, 1893 and 1905 are each attributed to
309 the central EAF on the basis of damage patterns and — in the earliest of these events
310 — reports of surface rupturing (Ambraseys, 1989). The May 3 1874 ($M \sim 7.1$) and March
311 27 1875 ($M \sim 6.7$) Gölcük Gölü earthquakes were both centered upon Lake Hazar, whose
312 former name they bear (Figure 1c). The 1874 earthquake devastated settlements along
313 a ~ 50 km corridor extending from Uslu, ~ 15 km west of the lake, to Tenik, ~ 20 km east
314 of it. Surface rupturing is suspected from reports that the south side of the lake was up-
315 lifted by ~ 1 – 2 m and that the valley NE of the lake was “rent” (Ambraseys, 1989; Am-
316 braseys & Jackson, 1998). The reported damage distribution hints that faulting may have
317 extended west of the lake, too, but this cannot be confirmed. It is therefore unclear whether
318 the 2020 earthquake ruptured into the slip area of the 1874 earthquake, or stopped short
319 of it. The 1875 earthquake was assigned the same macroseismic epicenter as the 1874
320 event, but its rupture extents are poorly constrained. The March 2 1893 ($M \sim 7.1$) and
321 December 4 1905 (M_s 6.8) Malatya earthquakes were both centered on the Yarpuzlu re-
322 straining bend, with damage focused upon settlements between Erkenek (in the west)
323 and Pürtürge (in the east) (Ambraseys, 1989). The eastern limit to the zone of maximum
324 damage in both earthquakes therefore approximates the western limit of faulting in the
325 2020 earthquake. However, without more precise information on the fault extents of the

1893 and 1905 earthquakes, it is unclear whether they are separated from, connected to, or partially overlap with the 2020 rupture area.

Duman and Emre (2013) used the apparent spatial separation between the 1875 and 1893 ruptures to argue for a seismic gap along the Pütürge segment of the EAF. However, our relocation of background seismicity marks this as amongst the most seismically active EAF segments in the past few decades, not normally the hallmark of a supposed seismic gap. During the period 1964–2019, the Pütürge segment hosted eight earthquakes large enough ($M_w > \sim 5$) to be ascribed teleseismic focal mechanisms, more than any other EAF segment (Figure 1b). Similarly, Bulut et al. (2012) observed that between 2007 and 2011 — and discounting the aftershock zone of the 2010 M_w 6.1 Kovancılar earthquake — the densest activity of small-to-moderate events ($M_w > \sim 3$) along the whole EAF occurred between Pütürge and Lake Hazar: the eventual 2020 rupture zone.

4.2 Earthquake behaviour and structural maturity

Our coseismic InSAR modeling suggests that only $\sim 20\%$ of the peak slip at depth reaches the surficial model fault patches, implying a shallow slip deficit of $\sim 80\%$ (Figure 3c). Other studies have shown that apparent shallow slip deficits can arise from a lack of resolution in near field InSAR data or from model uncertainties at shallow depth (Xu et al., 2016; Huang et al., 2017). However, in our case, the absence of a clear surface rupturing signal in optical imagery or from the preliminary field reconnaissance by Çetin et al. (2020) implies that the deficit inferred from InSAR modeling is real.

Dolan and Haravitch (2014) compared shallow slip deficits of six $M_w > 7.1$ strike-slip earthquakes, and observed that those on immature faults — defined as having cumulative offsets of < 25 km — had smaller ratios of surface slip to deep slip (~ 50 – 60%) than those on mature faults (~ 85 – 95%). This is thought to reflect the progressive localization of slip as fault zones evolve over many earthquake cycles, with more of the shallow strain manifest as inelastic, distributed deformation along immature faults (e.g., Kaneko & Fialko, 2011; Zinke et al., 2015; Roten et al., 2017). Earthquakes somewhat smaller than the cut-off of M_w 7.1 considered by Dolan and Haravitch (2014) might have even more pronounced shallow slip deficits because of the scaling of moment magnitude with slip area. For example, the 2003 Bam and 2017 Jiuzhaigou earthquakes, both M_w 6.5, each had pronounced shallow slip deficits, exhibited minimal postseismic afterslip, and

357 ruptured structurally-immature faults (Fialko et al., 2005; Li et al., 2020). The central
358 EAF is well-established as of low-to-intermediate structural maturity, with total offsets
359 of $\sim 9\text{--}26$ km (Duman & Emre, 2013), providing a plausible explanation for the low ($\sim 20\%$)
360 ratio of surface slip to peak slip at depth. The small amounts (<15 cm) of observed shall-
361 low afterslip, slow (~ 2 km/s) rupture speed, and scattered aftershocks are also consis-
362 tent with relatively immature faults (e.g., Liu et al., 2003; Perrin et al., 2016; Li et al.,
363 2020). This strongly motivates studies that seek to characterize and quantify off-fault
364 deformation along the EAF, and future morphotectonic or paleoseismological investiga-
365 tions should be undertaken with the awareness that a large proportion of deformation
366 may be distributed away from the main fault trace.

367 Ultimately, the shallow slip deficit must eventually be recovered for long-term slip
368 to be conserved; we now consider how and when that might occur. Early, localized, shall-
369 low afterslip is limited to $<7\%$ of the maximum coseismic slip magnitude, accounting
370 only for a small portion of the deficit (Figure 4). More could be recovered by persistent
371 shallow creep during the interseismic period, especially since serpentinite-rich ophiolitic
372 rocks mapped near the Pürtürge segment could plausibly exhibit velocity-strengthening
373 frictional behavior (Khalifa et al., 2018; Karaođlan et al., 2013; Yılmaz, 1993). However,
374 afterslip decays rapidly and disappears completely by mid February (Figure S5), inconsis-
375 tent with persistent creep (e.g., akir et al., 2012). Ultimately, longer geodetic time-
376 series are probably required in order to determine whether aseismic processes might ac-
377 count for the shallow slip deficit, or whether the shallow part of the fault is locked (e.g.,
378 Fielding et al., 2009).

379 This raises the possibility that the shortfall in shallow slip could be recovered by
380 future earthquakes. For example, a deficit in surface slip observed in the 1981 M_w 7.1
381 Sirch earthquake on the Gowk fault in Iran was later accounted for by the shallower 1998
382 M_w 6.6 Fandoqa event (Berberian et al., 2001). To address whether 2020 rupture released
383 all the accumulated strain along the Pürtürge segment of the EAF and the expectation
384 of a larger or shallower event re-rupturing this section to fill the shallow slip deficit, we
385 consider it in the context of the characteristic earthquake model (Schwartz & Copper-
386 smith, 1984). If the 2020 rupture were characteristic, then average coseismic slip of ~ 1 m
387 coupled with strain accumulation rates of ~ 11 mm/yr (Walters et al., 2014; Aktug et
388 al., 2016) would imply an average repeat interval of just ~ 90 years. While this approx-
389 imates the time since large earthquakes in 1874, 1893 and 1905, these historical events

390 were centered on adjacent segments of the EAF and likely did not rupture the entire Pürtürge
391 segment (Ambraseys, 1989; Ambraseys & Jackson, 1998). Moreover, a $\sim 3,800$ year record
392 of turbidites in Lake Hazar are interpreted to indicate a ~ 190 year average recurrence
393 interval that captures large events on both the Pürtürge and Palu segments of the EAF
394 (Hubert-Ferrari et al., 2020). This implies either that the 2020 M_w 6.8 earthquake was
395 not characteristic and that larger ruptures are possible. Future seismic hazard assess-
396 ments of the EAF should take into account this possibility.

397 5 Conclusions

398 The January 24 2020 M_w 6.8 Elazığ ruptured the Pürtürge segment of the EAF from
399 a nucleation point near an abrupt, $\sim 10^\circ$ bend in the fault surface trace. It was preceded
400 by two nearby (~ 5 km distance) moderate foreshocks on April 4 and December 27 2019.
401 ENE of the epicenter, the mainshock may have propagated into the rupture zone of the
402 1874 $M \sim 7.1$ Gölcük Gölü earthquake, and it halted in the Lake Hazar basin, previously
403 identified as a major EAF segment boundary. Towards the WSW, it propagated at ~ 2 km/s
404 and terminated after ~ 20 s along a straight, structurally-simple section of the Pürtürge
405 fault segment; relations with the 1893 $M \sim 7.1$ and 1905 M_s 6.9 Malatya earthquakes
406 are unclear. Overall, our results indicate that previous structural segmentation models
407 of the central EAF are oversimplified and that this was not a characteristic earthquake.
408 The mainshock rupture exhibits a pronounced shallow slip deficit, which is only partially
409 recovered through shallow afterslip. These characteristics — as well as the slow rupture
410 propagation speed and abundant off-fault background and aftershock seismicity — prob-
411 ably reflect the low-to-moderate structural maturity of the central EAF. The possibil-
412 ity for significant off-fault deformation should be taken into account in future paleoseis-
413 mological and morphotectonic studies of the EAF.

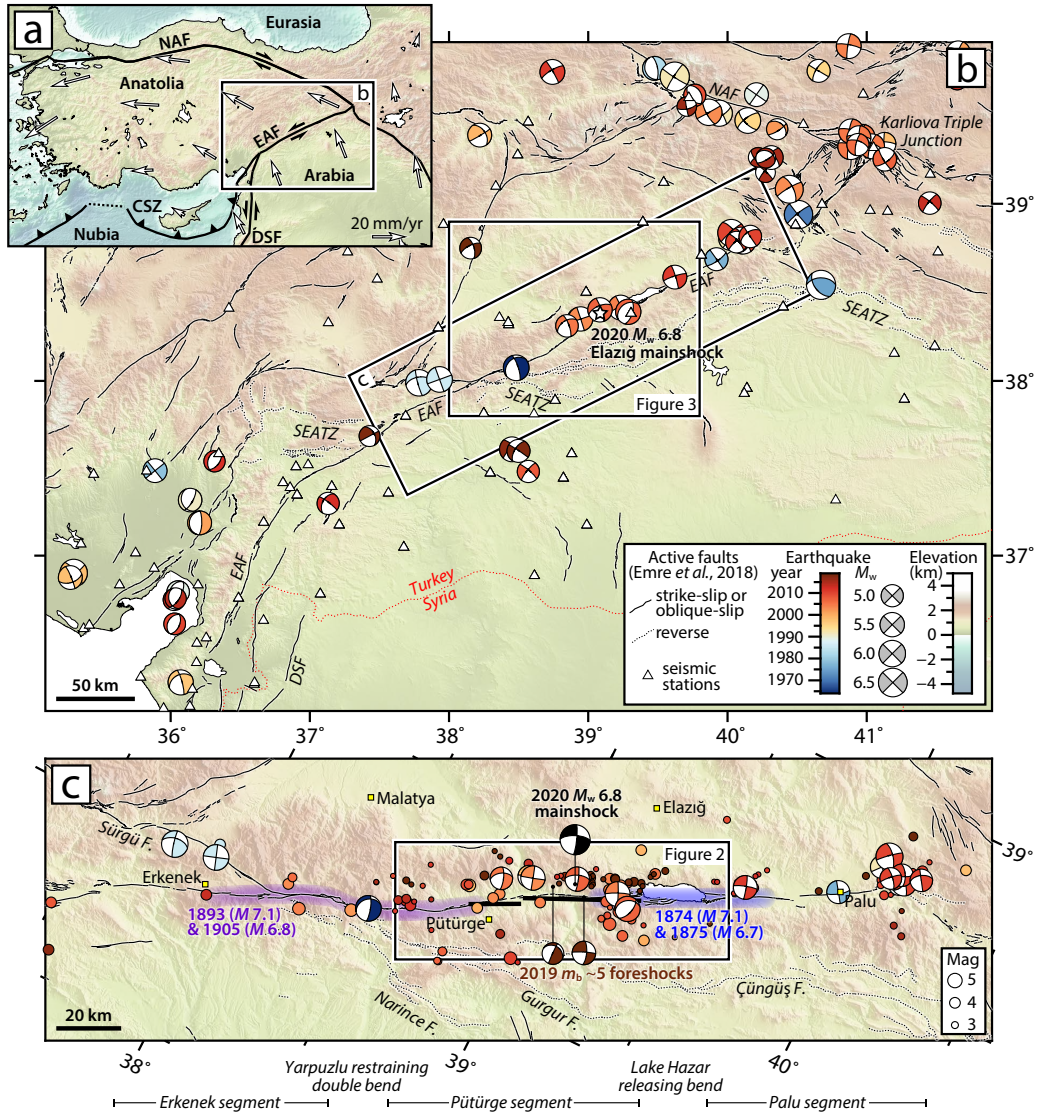


Figure 1. (Caption next page.)

Figure 1. (Previous page.) (a) Tectonic setting with plate boundaries (black lines) and representative GPS velocities relative to stable Eurasia (white arrows, from Kreemer et al. (2014)). CSZ = Cyprus Subduction Zone, DSF = Dead Sea Fault, EAF = East Anatolian Fault, NAF = North Anatolian Fault. (b) Focal mechanisms, station distribution, and active faults in SE Anatolia (SEATZ = Southeast Anatolia Thrust Zone). Teleseismic focal mechanisms, colored by year up to 2019, are from McKenzie (1972), Taymaz et al. (1991) and the U.S. Geological Survey (USGS) and Global Centroid Moment Tensor (GCMT) catalogs. We use our own, relocated epicenters along the EAF and ISC-EHB epicenters elsewhere (Weston et al., 2018). Triangles are seismic stations used for direct calibration of our relocation clusters and for regional waveform modeling. (c) Close-up of the central EAF. Colored shading shows zones of maximum damage associated with historical earthquakes in 1874 and 1875 (blue) and 1893 and 1905 (purple), from Ambraseys (1989). Focal mechanisms are as in (b) with the addition of two 2019 foreshocks and the 2020 Elazığ mainshock. Circles show earthquakes without focal mechanisms, colored the same but scaled differently. Thick black lines are surface projections of our preferred InSAR model faults for the 2020 mainshock. Below the map, we show the central EAF segmentation scheme of Duman and Emre (2013).

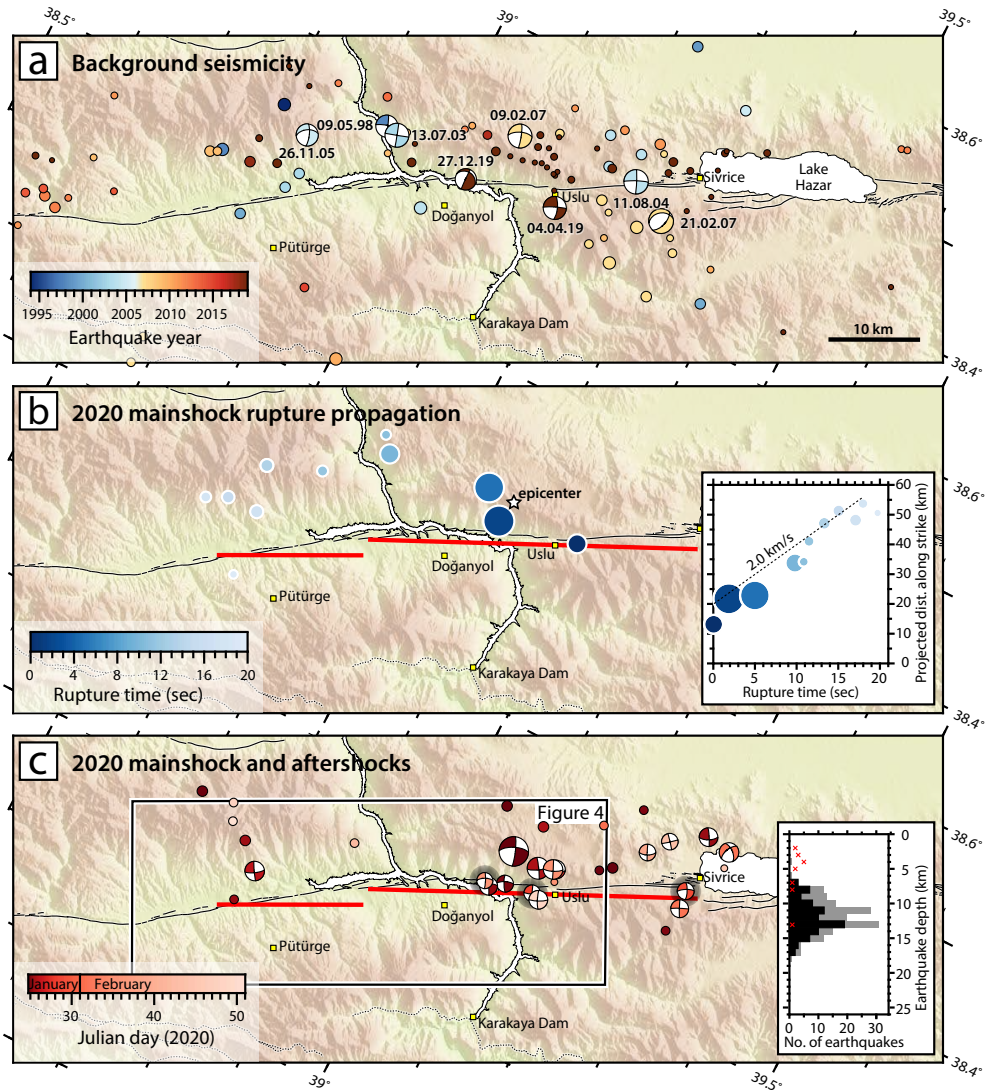


Figure 2. (Caption next page.)

Figure 2. (Previous page.) (a) Background seismicity (1994–2019) along the central and eastern Pürtürge segment of the EAF, plotted at relocated epicenters, colored by year, and scaled by magnitude as in Figure 1c. Focal mechanisms are from the GCMT and KOERI catalogs. Faults are as in Figure 1b–c. (b) Back projection results, scaled by relative energy and colored by rupture time. Thick red lines are surface projections of our preferred InSAR model faults for the 2020 Elazığ mainshock. Inset shows sub-event distance along strike versus rupture time, with distances projected onto a line of strike 244° and 0 km marking the eastern end of the InSAR model fault. (c) Elazığ mainshock and aftershock seismicity, colored by date and plotted at our relocated epicenters where possible (shadowed mechanisms are plotted at EMSC locations). The mainshock mechanism is from the GCMT catalog; aftershocks are best double couple solutions our own regional waveform modeling. Inset shows relocated focal depths of our local clusters, with 2019–2020 events in black and older events in gray. Red crosses show aftershock centroid depths from regional waveform modeling.

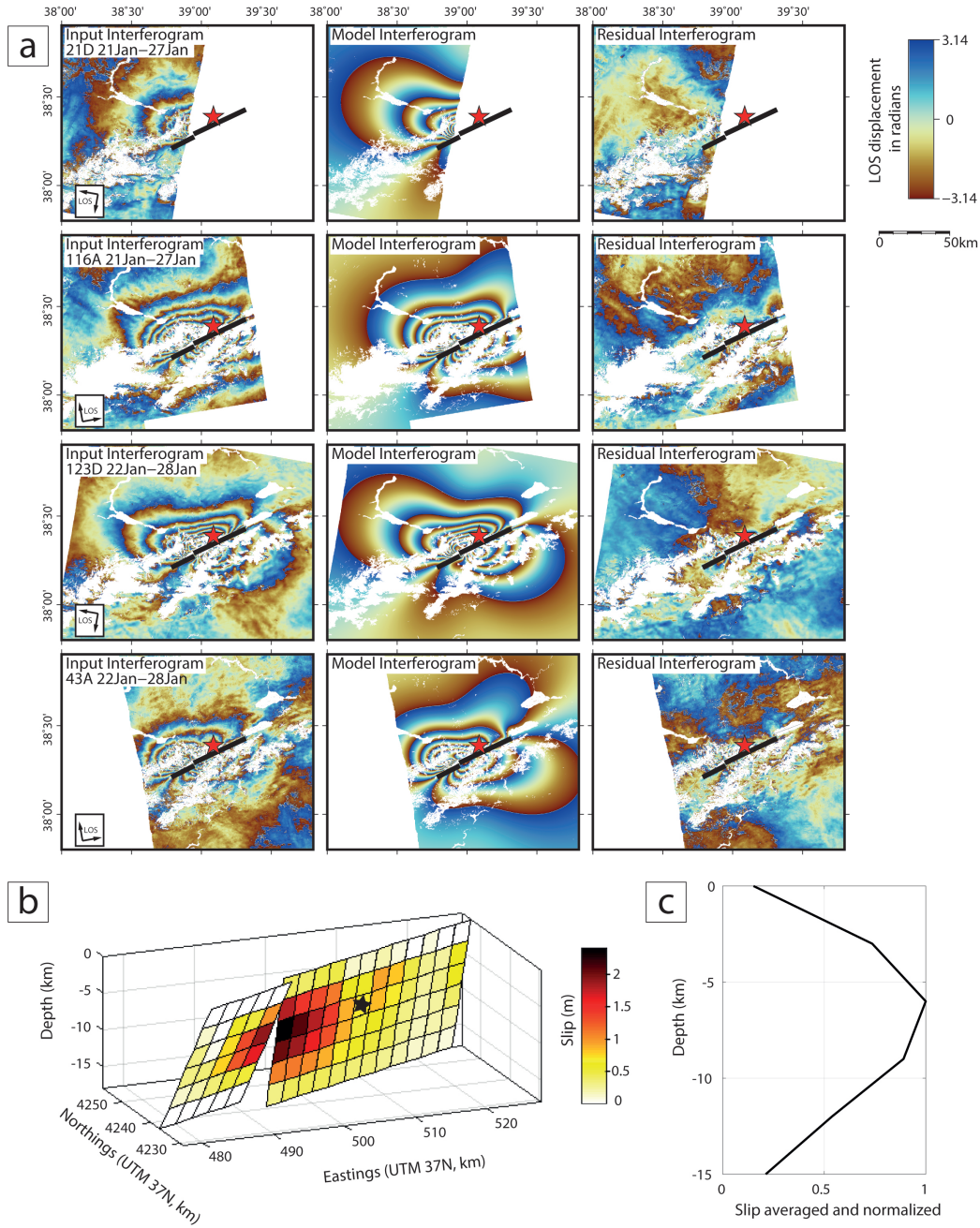


Figure 3. (a) From top to bottom: interferograms on track 21D, 116A, 123D and 43A. From left to right: observed, model and residual interferograms. Modeling was performed using unwrapped interferograms but the results are shown re-wrapped in order to accentuate deformation gradients and facilitate comparisons with data. The thick black line is the surface projection of the model faults and the red star is the relocated epicenter. (b) Model slip distribution. Each fault patch measures 3×3 km. The black star shows the relocated hypocenter at 8 km depth, projected on the fault plane. (c) Distribution of normalized average slip versus depth.

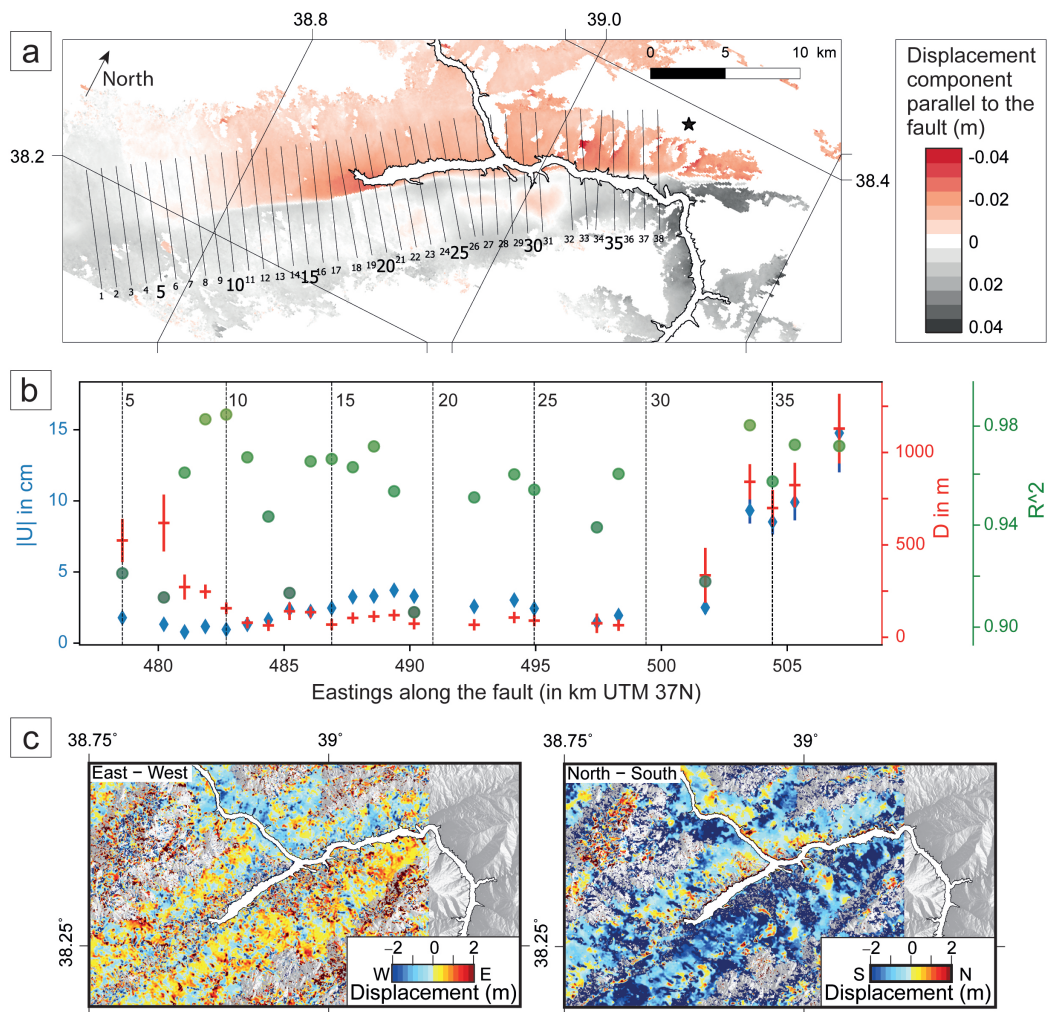


Figure 4. (a) Horizontal displacements projected onto the fault-parallel direction (244°) during the early postseismic period (January 27–February 21 2020), estimated from tracks 43A and 123D. The black star is the relocated epicenter. Profile lines 1 to 38 were used to fit our after-slip model. We only used profiles with more than 75% of data available. Observed and modeled profiles are plotted in Figure S6b. (b) Afterslip modeling results. Blue diamonds are slip U , red crosses are locking depth D , and green dots show coefficients of determination R^2 (only results with $R^2 > 0.9$ are shown). Vertical dashed lines labelled with numbers (5, 10, etc.) refer to profile numbers displayed in (a). (c) Horizontal (left) E–W and (right) N–S coseismic-to-early postseismic displacements mapped from optical image correlation (OIC) of Sentinel-2 images acquired on November 9 2019 and February 27 2020.

Table 1. Source parameters of the 2020 Elazığ mainshock. GCMT = Global Centroid Moment Tensor project; USGS = United States Geological Survey Comprehensive Earthquake Catalog; Mww = *W*-phase moment tensor; Mwr = regional moment tensor; Mwb = body wave tensor; AFAD = Disaster and Emergency Management Authority of Turkey; KOERI = Kandilli Observatory and Earthquake Research Institute. Lon. and lat. refer to the longitude and latitude of the InSAR model fault center surface projections, the GCMT centroid, and the USGS epicenter. Depth refers to the peak slip depth of the InSAR model and the centroid depth of the GCMT, USGS and KOERI solutions; AFAD list both the centroid and focal depths.

Source	Lon.	Lat.	Strike	Dip	Rake	Depth	Seismic moment	M_w
<i>This study</i>								
Eastern model fault	39.0648°	38.3363°	245°	80°	3°	6-9 km	1.36×10^{19} Nm	6.7
Western model fault	38.9349°	38.2655°	243°	64°	-18°	6-9 km	0.44×10^{19} Nm	6.4
<i>Other mechanisms</i>								
GCMT	39.00°	38.30°	246°	67°	-9°	12 km	1.77×10^{19} Nm	6.8
USGS Mww	39.088°	38.390°	245°	80°	-12°	22 km	1.39×10^{19} Nm	6.7
USGS Mwr	39.088°	38.390°	246°	77°	0°	11 km	0.60×10^{19} Nm	6.5
USGS Mwb	39.088°	38.390°	250°	85°	1°	16 km	1.23×10^{19} Nm	6.7
AFAD	39.0630°	38.3593°	248°	76°	1°	8/15 km	–	6.8
KOERI	39.29°	38.52°	248°	87°	-4°	10 km	1.29×10^{19} Nm	6.7

414 Acknowledgments

415 The University of Victoria Earthquakes group are supported by the Natural Sciences and
 416 Engineering Research Council of Canada, the Canada Foundation for Innovation, the BC
 417 Knowledge Development Fund, a Canada Research Chair to E. N., and an NSERC Alexan-
 418 der Graham Bell Canada Graduate Scholarship to E. G. All data used in this study are
 419 freely available through the links listed below. We used Copernicus Sentinel-1 InSAR
 420 and Sentinel-2 optical imagery (<https://scihub.copernicus.eu/>). Teleseismic wave-
 421 form data were obtained from IRIS Data Services, and specifically the IRIS Data Man-
 422 agement Center (<https://ds.iris.edu/ds/nodes/dmc/>), which are funded through the
 423 Seismological Facilities for the Advancement of Geoscience and EarthScope (SAGE) Pro-
 424 posal of the National Science Foundation (EAR-1261681). Regional waveforms were ob-
 425 tained from KOERI <http://eida-service.koeri.boun.edu.tr>. Arrival time data were
 426 obtained from the ISC Bulletin (<https://doi.org/10.31905/D808B830>). Our reloca-
 427 tion clusters have been added to the Global Catalog of Calibrated Earthquake Locations
 428 (<https://www.sciencebase.gov/catalog/item/59fb91fde4b0531197b16ac7>), where
 429 additional station maps and travel time residual plots are available. We used supplemen-
 430 tary location parameters from the relocated ISC-EHB dataset ([https://doi.org/10.31905/](https://doi.org/10.31905/PY08W6S3)
 431 [PY08W6S3](https://doi.org/10.31905/PY08W6S3)), and focal mechanisms from the GCMT project ([https://www.globalcmt](https://www.globalcmt.org/)
 432 [.org/](https://www.globalcmt.org/)), the USGS Comprehensive Earthquake Catalog ([https://earthquake.usgs.gov/](https://earthquake.usgs.gov/data/comcat/)
 433 [data/comcat/](https://earthquake.usgs.gov/data/comcat/)), AFAD (<https://deprem.afad.gov.tr/?lang=en>) and KOERI. Fig-
 434 ures were plotted with *Generic Mapping Tools* software (Wessel et al., 2013).

435 References

- 436 Acaarel, D., Cambaz, M. D., Turhan, F., Mutlu, A. K., & Polat, R. (2019). Seismo-
 437 tectonics of Malatya Fault, Eastern Turkey. *Open Geosciences*, *11*(1).
- 438 Aksoy, E., Inceoez, M., & Köçyiğit, A. (2007). Lake Hazar basin: A negative
 439 flower structure on the east anatolian fault system (EAFS), SE Turkey.
 440 *Turk. J. Earth Sci.*, *16*(3), 319–338.
- 441 Aktug, B., Ozener, H., Dogru, A., Sabuncu, A., Turgut, B., Halicioglu, K., ... Hava-
 442 zli, E. (2016). Slip rates and seismic potential on the East Anatolian Fault
 443 System using an improved GPS velocity field. *J. Geodynamics*, *94*, 1–12.
- 444 Ambraseys, N. N. (1989). Temporary seismic quiescence: SE Turkey. *Geo-*
 445 *phys. J. Int.*, *96*(2), 311–331.

- 446 Ambraseys, N. N., & Jackson, J. A. (1998). Faulting associated with historical and
 447 recent earthquakes in the Eastern Mediterranean region. *Geophys. J. Int.*, *133*,
 448 390–406.
- 449 Arpat, E., & Şaroğlu, F. (1972). Some observations and thoughts on the East Ana-
 450 tolian fault. *Bull. Miner. Res. Explor. Inst. Turkey*, *73*, 44–50.
- 451 Ayoub, F., Leprince, S., & Avouac, J.-P. (2017). User’s guide to COSI-CORR
 452 co-registration of optically sensed images and correlation [Computer software
 453 manual].
- 454 Barka, A. (1996). Slip distribution along the North Anatolian fault associated with
 455 the large earthquakes of the period 1939 to 1967. *Bull. Seismol. Soc. Am.*,
 456 *86*(5), 1238–1254.
- 457 Barka, A. A., & Kadinsky-Cade, K. (1988). Strike-slip fault geometry in Turkey and
 458 its influence on earthquake activity. *Tectonics*, *7*(3), 663–684.
- 459 Berberian, M., Jackson, J. A., Fielding, E., Parsons, B. E., Priestley, K., Qorashi,
 460 M., . . . Baker, C. (2001, August). The 1998 March 14 Fandoqa earthquake
 461 (M_w 6.6) in Kerman province, southeast Iran: re-rupture of the 1981 Sirch
 462 earthquake fault, triggering of slip on adjacent thrusts and the active tectonics
 463 of the Gowk fault zone. *Geophys. J. Int.*, *146*, 371–398.
- 464 Bergman, E. A., & Solomon, S. C. (1990). Earthquake swarms on the Mid-Atlantic
 465 Ridge — Products of magmatism or extensional tectonics? *J. Geophys. Res.*,
 466 *95*, 4943–4965.
- 467 Bouchon, M. (1981). A simple method to calculate Green’s functions for elastic lay-
 468 ered media. *Bull. Seismol. Soc. Am.*, *71*(4), 959–971.
- 469 Boğaziçi University Kandilli Observatory and Earthquake Research Institute. (2001).
 470 *International Federation of Digital Seismograph Networks. Dataset/Seismic*
 471 *Network*. doi: 10.7914/SN/KO
- 472 Bozkurt, E. (2001). Neotectonics of Turkey — a synthesis. *Geodinamica Acta*, *14*(1),
 473 3–30.
- 474 Brodsky, E. E., Gilchrist, J. J., Sagy, A., & Collettini, C. (2011). Faults smooth
 475 gradually as a function of slip. *Earth Planet. Sci. Lett.*, *30*(1), 185–193.
- 476 Bulut, F., Bohnhoff, M., Eken, T., Janssen, C., Kılıç, T., & Dresen, G. (2012). The
 477 East Anatolian Fault Zone: Seismotectonic setting and spatiotemporal charac-
 478 teristics of seismicity based on precise earthquake locations. *J. Geophys. Res.*,

- 479 117.
- 480 Çakır, Z., Ergintav, S., Özener, H., Dogan, U., Akoglu, A. M., Meghraoui, M., &
 481 Reilinger, R. (2012). Onset of aseismic creep on major strike-slip faults.
 482 *Geology*, *40*(12), 1115–1118.
- 483 Cetin, H., Güneçli, H., & Mayer, L. (2003). Paleoseismology of the Palu-Lake Hazar
 484 segment of the East Anatolian Fault Zone, Turkey. *Tectonophys.*, *374*(3), 163–
 485 197.
- 486 Çetin, K. Ö., Ilgac, M., Can, G., Çakır, E., & Söylemez, B. (2020). *January 24,*
 487 *2020 Elazığ-Sivrice earthquake ($M_w=6.8$) Reconnaissance Study Report* (Tech.
 488 Rep. No. METU/EERC 2020-01). Middle East Technical University. doi:
 489 10.17603/ds2-9jz1-e287
- 490 Clarke, P. J., Paradissis, D., Briole, P., England, P. C., Parsons, B. E., Billiris, H.,
 491 ... Ruegg, J.-C. (1997). Geodetic investigation of the 13 May 1995 Kozani-
 492 Grevena (Greece) earthquake. *Geophys. Res. Lett.*, *24*, 707–710.
- 493 Şengör, A. M. C., & Yilmaz, Y. (1981). Tethyan evolution of Turkey: A plate tec-
 494 tonic approach. *Tectonophys.*, *75*(3), 181–241.
- 495 Diederichs, A., Nissen, E. K., Lajoie, L. J., Langridge, R. M., Malireddi, S. R.,
 496 Clark, K. J., ... Tagliasacchi, A. (2019). Unusual kinematics of the Papatea
 497 fault (2016 Kaikōura earthquake) suggest anelastic rupture. *Sci. Adv.*, *5*(10).
- 498 Dolan, J. F., & Haravitch, B. D. (2014). How well do surface slip measurements
 499 track slip at depth in large strike-slip earthquakes? The importance of fault
 500 structural maturity in controlling on-fault slip versus off-fault surface deforma-
 501 tion. *Earth Planet. Sci. Lett.*, *388*, 38–47.
- 502 Duman, T. Y., & Emre, O. (2013). The East Anatolian Fault: geometry, seg-
 503 mentation and jog characteristics. In A. H. F. Robertson, O. Parlak, &
 504 U. C. Ünlügenç (Eds.), *Geological Development of Anatolia and the East-*
 505 *ernmost Mediterranean Region* (Vol. 372, pp. 495–529). Geol. Soc. Lon-
 506 don Spec. Publ..
- 507 Elliott, J. R., Nissen, E. K., England, P. C., Jackson, J. A., Lamb, S., Li, Z., ...
 508 Parsons, B. (2012). Slip in the 2010-2011 Canterbury earthquakes, New
 509 Zealand. *J. Geophys. Res.*, *117*.
- 510 Fialko, Y., Sandwell, D., Simons, M., & Rosen, P. (2005). Three-dimensional de-
 511 formation caused by the Bam, Iran, earthquake and the origin of shallow slip

- 512 deficit. *Nature*, *435*, 295–299.
- 513 Fielding, E. J., Lundgren, P. R., Bürgmann, R., & Funning, G. J. (2009). Shallow
514 fault-zone dilatancy recovery after the 2003 Bam earthquake in Iran. *Nature*,
515 *458*(7234), 64–68.
- 516 Garcia Moreno, D., Hubert-Ferrari, A., Moernaut, J., Fraser, J. G., Boes, X., Van
517 Daele, M., . . . De Batist, M. (2011). Structure and recent evolution of the
518 Hazar Basin: a strike-slip basin on the East Anatolian Fault, Eastern Turkey.
519 *Basin. Res.*, *23*(2), 191–207.
- 520 Gaudreau, É., Nissen, E. K., Bergman, E. A., Benz, H. M., Tan, F., & Karasözen,
521 E. (2019). The August 2018 Kaktovik earthquakes: Active tectonics in north-
522 eastern Alaska revealed with InSAR and seismology. *Geophys. Res. Lett.*, *46*,
523 14412–14420.
- 524 Huang, M. H., Fielding, E. J., Dickinson, H., Sun, J., Gonzalez-Ortega, J. A., Freed,
525 A. M., & Bürgmann, R. (2017). Fault geometry inversion and slip distribu-
526 tion of the 2010 Mw 7.2 El Mayor-Cucapah earthquake from geodetic data.
527 *J. Geophys. Res.*, *122*(1), 607–621.
- 528 Hubert-Ferrari, A., Lamair, L., Hage, S., Schmidt, S., Namık Çağatay, M., & Avşar,
529 U. (2020, May). A 3800 yr paleoseismic record (Lake Hazar sediments,
530 eastern Turkey): Implications for the East Anatolian Fault seismic cycle.
531 *Earth Planet. Sci. Lett.*, *538*.
- 532 Ishii, M., Shearer, P. M., Houston, H., & Vidale, J. E. (2005). Extent, duration and
533 speed of the 2004 Sumatra-Andaman earthquake imaged by the Hi-Net array.
534 *Nature*, *435*, 933–936.
- 535 Jónsson, S., Zebker, H., Segall, P., & Amelung, F. (2002). Fault Slip Distribution of
536 the 1999 M_w 7.1 Hector Mine, California, Earthquake, Estimated from Satel-
537 lite Radar and GPS Measurements. *Bull. Seismol. Soc. Am.*, *92*, 1377–1389.
- 538 Jordan, T. H., & Sverdrup, K. A. (1981). Teleseismic location techniques and their
539 application to earthquake clusters in the South-Central Pacific. *Bull. Seis-
540 mol. Soc. Am.*, *71*, 1105–1130.
- 541 Kagan, Y. Y., Jackson, D. D., & Geller, R. J. (2012). Characteristic earthquake
542 model, 1884–2011, RIP. *Seismol. Res. Lett.*, *83*(6), 951–953.
- 543 Kaneko, Y., & Fialko, Y. (2011). Shallow slip deficit due to large strike-slip earth-
544 quakes in dynamic rupture simulations with elasto-plastic off-fault response.

- 545 *Geophys. J. Int.*, 186(3), 1389–1403.
- 546 Karaoğlan, F., Parlak, O., Klötzli, U., Koller, F., & Rızaoğlu, T. (2013). Age and
547 duration of intra-oceanic arc volcanism built on a suprasubduction zone type
548 oceanic crust in southern Neotethys, SE Anatolia. *Geosci. Frontiers*, 4(4),
549 399–408.
- 550 Karasözen, E., Nissen, E., Bergman, E. A., Johnson, K. L., & Walters, R. J. (2016).
551 Normal faulting in the Simav graben of western Turkey reassessed with cali-
552 brated earthquake relocations. *J. Geophys. Res.*, 121, 4553–4574.
- 553 Karasözen, E., Nissen, E., Büyükakpınar, P., Cambaz, M. D., Kahraman, M., Er-
554 tan, E. K., . . . Özacar, A. A. (2018). The 2017 July 20 M_w 6.6 Bodrum–Kos
555 earthquake illuminates active faulting in the Gulf of Gökova, SW Turkey.
556 *Geophys. J. Int.*, 214(1), 185–199.
- 557 Kennett, B. L. N., & Engdahl, E. R. (1991, May). Traveltimes for Global Earth-
558 quake Location and Phase Identification. *Geophys. J. Int.*, 105, 429–465.
- 559 Kennett, B. L. N., Engdahl, E. R., & Buland, R. (1995, July). Constraints on seis-
560 mic velocities in the Earth from traveltimes. *Geophys. J. Int.*, 122, 108–124.
- 561 Khalifa, A., Çakir, Z., Owen, L. A., & Kaya, Ş. (2018). Morphotectonic analysis of
562 the East Anatolian Fault, Turkey. *Turk. J. Earth Sci.*, 27, 110–126.
- 563 Kikuchi, M., & Kanamori, H. (1991). Inversion of complex body waves—iii.
564 *Bull. Seismol. Soc. Am.*, 81(6), 2335–2350.
- 565 Kreemer, C., Blewitt, G., & Klein, E. C. (2014). A geodetic plate motion and Global
566 Strain Rate Model. *gcubed*, 15(10), 3849–3889.
- 567 Leprince, S., Barbot, S., Ayoub, F., & Avouac, J.-P. (2007). Automatic and Precise
568 Orthorectification, Coregistration, and Subpixel Correlation of Satellite Im-
569 ages, Application to Ground Deformation Measurements. *IEEE Trans. Geosci.*
570 *Rem. Sens.*, 45, 1529–1558. doi: 10.1109/TGRS.2006.888937
- 571 Li, Y., Bürgmann, R., & Zhao, B. (2020). Evidence of Fault Immaturity from
572 Shallow Slip Deficit and Lack of Postseismic Deformation of the 2017 M_w 6.5
573 Jiuzhaigou Earthquake. *Bull. Seismol. Soc. Am.*, 110(1), 154–165.
- 574 Liu, J., Sieh, K., & Hauksson, E. (2003). A Structural Interpretation of the
575 Aftershock “Cloud” of the 1992 M_w 7.3 Landers Earthquake. *Bull. Seis-*
576 *mol. Soc. Am.*, 93(3), 1333–1344.
- 577 Manighetti, I., Campillo, M., Bouley, S., & Cotton, F. (2007, January). Earthquake

- 578 scaling, fault segmentation, and structural maturity. *Earth Planet. Sci. Lett.*,
579 *253*, 429–438.
- 580 McCann, W. R., Nishenko, S. P., Sykes, L. R., & Krause, J. (1979). Seismic gaps
581 and plate tectonics: seismic potential for major boundaries. In *Earthquake pre-*
582 *diction and seismicity patterns* (pp. 1082–1147). Springer.
- 583 McKenzie, D. (1972). Active Tectonics of the Mediterranean Region. *Geo-*
584 *phys. J. Int.*, *30*, 109–185.
- 585 Melgar, D., Ganas, A., Taymaz, T., Valkaniotis, S., Crowell, B. W., Kapetanidis,
586 V., . . . Öcalan, T. (2020). Rupture Kinematics of January 24, 2020 Mw
587 6.7 Doğanyol-Sivrice, Turkey Earthquake on the East Anatolian Fault Zone
588 Imaged by Space Geodesy. *EarthArXiv*. doi: 10.31223/osf.io/xzg9c
- 589 Moré, J. J. (1978). The Levenberg-Marquardt algorithm: Implementation and the-
590 ory. In G. A. Watson (Ed.), *Numerical analysis* (pp. 105–116). Springer Berlin
591 Heidelberg.
- 592 Okada, Y. (1985). Surface deformation due to shear and tensile faults in a half-
593 space. *Bull. Seismol. Soc. Am.*, *75*, 1135–1154.
- 594 Perrin, C., Manighetti, I., Ampuero, J.-P., Cappa, F., & Gaudemer, Y. (2016). Lo-
595 cation of largest earthquake slip and fast rupture controlled by along-strike
596 change in fault structural maturity due to fault growth. *J. Geophys. Res.*, *121*,
597 3666–3685.
- 598 Press, W. H., Teukolsky, S. A., Vetterling, W. T., & Flannery, B. P. (1992). *Numer-*
599 *ical recipes in c: The art of scientific computing*. Cambridge: Cambridge Uni-
600 versity Press.
- 601 Roten, D., Olsen, K., & Day, S. (2017). Off-fault deformations and shallow slip
602 deficit from dynamic rupture simulations with fault zone plasticity. *Geo-*
603 *phys. Res. Lett.*, *44*(15), 7733–7742.
- 604 Savage, H. M., & Brodsky, E. E. (2011). Collateral damage: Evolution with dis-
605 placement of fracture distribution and secondary fault strands in fault damage
606 zones. *J. Geophys. Res.*, *116*.
- 607 Savage, J. C., & Burford, R. O. (1973). Geodetic determination of relative plate
608 motion in central California. *J. Geophys. Res.*, *78*(5), 832–845. doi: 10.1029/
609 JB078i005p00832
- 610 Schwartz, D. P., & Coppersmith, K. J. (1984, July). Fault behavior and character-

- 611 istic earthquakes: Examples from the Wasatch and San Andreas Fault Zones.
612 *J. Geophys. Res.*, *89*(B7), 5681–5698.
- 613 Shelef, E., & Oskin, M. (2010). Deformation processes adjacent to active faults: Ex-
614 amples from eastern California. *J. Geophys. Res.*, *115*.
- 615 Socquet, A., Hollingsworth, J., Pathier, E., & Bouchon, M. (2019). Evidence of su-
616 pershear during the 2018 magnitude 7.5 Palu earthquake from space geodesy.
617 *Nat. Geosci.*, *12*(3), 192–199.
- 618 Sokos, E., & Zahradník, J. (2013). Evaluating Centroid-Moment-Tensor Uncertainty
619 in the New Version of ISOLA Software. *Seismol. Res. Lett.*, *84*(4), 656–665.
- 620 Sokos, E. N., & Zahradník, J. (2008). ISOLA a Fortran code and a Matlab GUI
621 to perform multiple-point source inversion of seismic data. *Computers & Geo-*
622 *sciences*, *34*, 967–977.
- 623 Tan, F., Ge, Z., Kao, H., & Nissen, E. (2019). Validation of the 3-D phase-weighted
624 relative back projection technique and its application to the 2016 M_w 7.8
625 Kaikōura earthquake. *Geophys. J. Int.*, *217*(1), 375–388.
- 626 Tan, O., Pabuçcu, Z., Tapırdamaz, M. C., İnan, S., Ergintav, S., Eyidoğan, H., . . .
627 Kuluöztürk, F. (2011). Aftershock study and seismotectonic implications
628 of the 8 March 2010 Kovancılar (Elazığ, Turkey) earthquake ($M_W = 6.1$).
629 *Geophys. Res. Lett.*, *38*(11).
- 630 Taymaz, T., Eyidoğan, H., & Jackson, J. (1991). Source parameters of large earth-
631 quakes in the East Anatolian Fault Zone (Turkey). *Geophys. J. Int.*, *106*(3),
632 537–550.
- 633 Tibi, R., Bock, G., Xia, Y., Baumbach, M., Grosser, H., Milkereit, C., . . . Zschau,
634 J. (2001). Rupture processes of the 1999 August 17 Izmit and November 12
635 Düzce (Turkey) earthquakes. *Geophys. J. Int.*, *144*(2), F1–F7.
- 636 Walker, R. T., Bergman, E. A., Szeliga, W., & Fielding, E. J. (2011). Insights
637 into the 1968–1997 Dasht-e-Bayaz and Zirkuh earthquake sequences, eastern
638 Iran, from calibrated relocations, InSAR and high-resolution satellite imagery.
639 *Geophys. J. Int.*, *187*, 1577–1603.
- 640 Walters, R. J., Parsons, B., & Wright, T. J. (2014). Constraining crustal velocity
641 fields with InSAR for Eastern Turkey: Limits to the block-like behavior of
642 Eastern Anatolia. *J. Geophys. Res.*, *119*(6), 5215–5234.
- 643 Wesnousky, S. G. (1988). Seismological and structural evolution of strike-slip faults.

- 644 *Nature*, 335(6188), 340–343.
- 645 Wessel, P., Smith, W. H. F., Scharroo, R., Luis, J., & Wobbe, F. (2013). Generic
646 Mapping Tools: Improved Version Released. *Eos Trans. AGU*, 94, 409–410.
- 647 Weston, J., Engdahl, E. R., Harris, J., Di Giacomo, D., & Storchak, D. A. (2018).
648 ISC-EHB: reconstruction of a robust earthquake data set. *Geophys. J. Int.*,
649 214(1), 474–484.
- 650 Wright, T. J., Lu, Z., & Wicks, C. (2003). Source model for the M_w 6.7, 23
651 October 2002, Nenana Mountain Earthquake (Alaska) from InSAR. *Geo-*
652 *phys. Res. Lett.*, 30(18).
- 653 Wright, T. J., Parsons, B. E., Jackson, J. A., Haynes, M., Fielding, E. J., England,
654 P. C., & Clarke, P. J. (1999). Source parameters of the 1 October 1995
655 Dinar (Turkey) earthquake from SAR interferometry and seismic bodywave
656 modelling. *Earth Planet. Sci. Lett.*, 172, 23–37.
- 657 Wright, T. J., Parsons, B. E., & Lu, Z. (2004). Toward mapping surface deformation
658 in three dimensions using InSAR. *Geophys. Res. Lett.*, 31.
- 659 Xu, X., Tong, X., Sandwell, D. T., Milliner, C. W. D., Dolan, J. F., Hollingsworth,
660 J., ... Ayoub, F. (2016). Refining the shallow slip deficit. *Geophys. J. Int.*,
661 204(3), 1867–1886.
- 662 Yılmaz, Y. (1993). New evidence and model on the evolution of the southeast Ana-
663 tolian orogen. *Geol. Soc. Am. Bull.*, 105(2), 251–271.
- 664 Zahradník, J., & Sokos, E. (2018). ISOLA Code for Multiple-Point Source Model-
665 ing—Review. In S. Damico (Ed.), *Moment tensor solutions*. Springer, Cham.
- 666 Zinke, R., Dolan, J. F., Van Dissen, R., Grenader, J. R., Rhodes, E. J., McGuire,
667 C. P., ... Hatem, A. E. (2015). Evolution and progressive geomorphic mani-
668 festation of surface faulting: A comparison of the Wairau and Awatere faults,
669 South Island, New Zealand. *Geology*, 43(11), 1019–1022.